PTEP

Prog. Theor. Exp. Phys. **2020**, 103E01 (24 pages)
DOI: 10.1093/ptep/ptaa126

# Analytic properties of the electromagnetic field of binary compact stars and electromagnetic precursors to gravitational waves

Tomoki Wada[1,*,†], Masaru Shibata[1,2], and Kunihito Ioka[1]

[1]*Center for Gravitational Physics, Yukawa Institute for Theoretical Physics, Kyoto University, Kyoto, 606-8502, Japan*
[2]*Max Planck Institute for Gravitational Physics (Albert Einstein Institute), Am Mühlenberg 1, Potsdam-Golm, 14476, Germany*
[*]E-mail: tomoki.wada@yukawa.kyoto-u.ac.jp
[†]JSPS Research Fellow.

Received June 1, 2020; Revised August 6, 2020; Accepted August 11, 2020; Published October 24, 2020

We analytically study the properties of the electromagnetic field in the vacuum around close binary compact stars containing at least one neutron star. We show that the orbital motion of the neutron star induces high multipole modes of the electromagnetic field just before the merger. These modes are superimposed to form a spiral arm configuration, and its edge is found to be a likely site for magnetic reconnection. These modes also enhance the total Poynting flux from neutron star binaries by a factor of 2–4. We also indicate that the electric field induced by the orbital motion leads to a magnetosphere around binaries and estimate its plasma density, which has a different parameter dependence than the Goldreich–Julian density. With these properties, we discuss possible electromagnetic counterparts to gravitational wave events, and identify radio precursors, such as fast radio bursts, as the most promising observational targets.

Subject Index E01, E02, E32, E38

## 1. Introduction

In August 2017, gravitational waves from a binary neutron star (BNS) merger, GW170817, and its electromagnetic counterparts, GRB170817A and AT2017 gfo, were observed by aLIGO/VIRGO and many telescopes [1–3]. This event had a lot of implications for astrophysics and gravitational physics; for example, the origin of short gamma-ray bursts [4–6], the origin of *r*-process elements [7], estimation of the Hubble constant [8,9], and the speed of gravitational waves [10,11]. This discovery showed that multi-messenger astronomy of gravitational-wave and electromagnetic-wave observations contributes to answering many unsolved issues. In the aLIGO/VIRGO O3 run, one gravitational-wave event, GW190425, has so far been reported [12]. There are several other candidates for BNS mergers and black hole–neutron star (BH–NS) mergers.

Many models have been suggested for electromagnetic counterparts of neutron-star (NS) mergers (for a review, see Refs. [13–15]). A short gamma-ray burst [4,16], its afterglow [17], and a kilonova/macronova [18,19] have been detected in GW170817. However, there might be other electromagnetic counterparts. One candidate is late-time engine activity driven by fall-back accretion to the central black hole [20] or by the spin-down luminosity of the magnetar formed after the merger of a BNS. Another candidate is an electromagnetic precursor driven by the orbital motion or magnetospheric interaction of the NSs.

There are several precursor models: dipole radiation [21], dipole radiation from charged compact binaries [22], a DC circuit (unipolar induction) [23–28], the interaction of magnetospheres [29–36], and the fireball model [28,37]. The physical process that takes place before the merger, and physical quantities such as the strength of the magnetic field of the NS(s) in binaries, are not well understood. Furthermore, because the electromagnetic precursor is radiated before the merger, it is not easy to detect it. However, in the era of space-based gravitational wave detectors, namely Laser Interferometer Space Antenna (LISA) [38], the sky position will be predicted before the merger [39] and then the electromagnetic precursor will be a new target for observations. If DECi-hertz Interferometer Gravitational wave Observatory (DECIGO) [40,41], or similar detectors that have sensitivity below 10 Hz, such as TaiJi [42] and TianQin [43], are realized, we will have more opportunities to observe electromagnetic precursors of NS mergers.

In this paper we analytically study the properties of the electromagnetic field in the vacuum around a binary system of compact stars containing at least one NS. In compact NS binaries, the velocity of the compact objects just before the merger is 30%–40% of the speed of light, and we have to take the special relativistic effects on the electromagnetic field into account. Motivated by this fact, we analytically solve the Maxwell equations in a vacuum using the vector harmonics expansion, which retains the special relativistic correction in a straightforward manner. First, we show the analytic solution for the vacuum electromagnetic field induced by a moving magnetic dipole, and display the configuration of the electromagnetic field. With this analytic solution, we calculate the total Poynting flux radiated from binaries, and show that the special relativistic effect enhances the Poynting flux. Second, we indicate that the orbital motion of an NS can induce a magnetosphere around the binary, and estimate the number density of the plasma to explore its plasma effect on the electromagnetic precursor of binary mergers. Third, we discuss the observability of precursors of binary mergers, assuming that the emission would be similar to that from pulsars.

In this study we only consider the vacuum case without plasma. In some numerical simulations, the plasma effects have been taken into account. For example, a resistive magnetohydrodynamic simulation for the electromagnetic field around binary compact stars was performed in Refs. [31,32]. A particle-in-cell simulation without the orbital motion of binaries was performed in Ref. [35]. Force-free simulations of an NS binary were performed in Refs. [36,44]. These simulations show the luminosity from binaries with plasma for a few milliseconds before the merger. We analytically derive a radiation formula which clarifies the dependence of the luminosity on the orbital separation of binaries and on other parameters (e.g. the mass, radius, and magnetic field of the compact stars). Thus, our work is complementary to these previous works. Also, our calculation contains the special relativistic effect that enhances the Poynting flux from the binary, especially just before the merger. In Ref. [21], the Poynting flux is calculated in zeroth order of $v/c$ (where $v$ is the velocity of the NS and $c$ is the speed of light). Our analytic treatment makes it possible to calculate the Poynting flux in a series of $v/c$. The higher-order terms enhance the Poynting flux by a factor of 2–4. Our analytic results are consistent with the numerical result of Ref. [44].

The paper is organized as follows. In Sect. 2 we show the exact solution of the electromagnetic field induced by a magnetic dipole moment orbiting the companion (NS or BH). Motivated by the fact that some pulsars are considered to release particle wind, or to radiate coherent radio waves via the magnetic reconnection process in their current sheets [45–47], we speculate on the location of magnetic reconnection induced by the orbital motion of the NS if plasma exists. We also evaluate the effect of the higher multipole modes on the total luminosity. In Sect. 3 we first indicate that the orbital motion of a magnetized NS induces a magnetosphere around the NS. Then, we study

the observability of the precursor as an electromagnetic counterpart of binary mergers. Section 4 is devoted to a summary and discussion.

## 2. Electromagnetic field around an NS binary

In this section we consider the electromagnetic field induced by the orbital motion of a magnetized NS in a compact binary system. We consider the case in which the binary contains at least one magnetized NS and is in a late inspiral phase a few milliseconds before the merger. For simplicity, we assume that the NS is orbiting its companion in Kepler motion. We also assume that the NS does not have an intrinsic spin. The former assumption is reasonable during the inspiral phase, that is, until the binary separation reaches the innermost stable circular orbit (ISCO) of the companion [48,49]. The latter is justified in the late inspiral phase. This is because tidal locking is not effective and, just before the merger, the orbital velocity is usually much higher than the spin velocity of the NS [50]. Also, we use a dipole approximation for the magnetic field of the NS. In this section we use units in which $G = 1$ and $c = 1$, where $G$ is the gravitational constant.

With these assumptions, we consider the electromagnetic field induced by the orbiting magnetic dipole moment. The mass of the NS is $M_{\rm NS}$, the mass of the companion is $M_{\rm c}$, and the separation of the binary is $R$. Also, the total mass is $M(= M_{\rm NS} + M_{\rm c})$, and the distance between the NS and the center-of-mass of the binary is $a$ $(= RM_{\rm c}/M)$. The binary orbital motion is in the $x$–$y$ plane. Then, in Cartesian coordinates, the NS is at

$$\vec{r}_{\rm NS}(t) = (a\cos\Omega t,\ a\sin\Omega t,\ 0), \tag{1}$$

where $\Omega = \sqrt{\frac{M_{\rm NS}+M_{\rm c}}{R^3}}$ is the angular velocity and $t$ is the time in the center-of-mass frame.

### 2.1. *Vector harmonics expansion and the exact solution of the electromagnetic field*

The definition of the vector spherical harmonics expansion of a vector $\vec{B}$ is [51]

$$\vec{B} = \sum_{l,m}\left[B_1^{lm}\left(Y_{lm}(\theta,\phi),0,0\right) + B_2^{lm}\left(0,\frac{1}{r}Y_{lm,\theta}(\theta,\phi),\frac{1}{r\sin\theta}Y_{lm,\phi}(\theta,\phi)\right)\right.$$
$$\left. + B_3^{lm}\left(0,-\frac{1}{r}\frac{Y_{lm,\phi}(\theta,\phi)}{\sin\theta},\frac{1}{r\sin\theta}\sin\theta\, Y_{lm,\theta}(\theta,\phi)\right)\right], \tag{2}$$

where each vector component represents the $r,\theta,\phi$ component in polar coordinates, $Y_{lm}(\theta,\phi)$ is the $l,m$ component of the spherical harmonics, a comma in the subscript denotes the partial derivative ($_{,\theta} = \partial_\theta$, $_{,\phi} = \partial_\phi$), and $B_1^{lm}$, $B_2^{lm}$, and $B_3^{lm}$ are functions of $t$ and $r$. Using these expressions, we rewrite the Maxwell equations in terms of $B_i^{lm}$ and $E_i^{lm}$ $(i = 1,2,3)$ in polar coordinates. The time evolution of the magnetic fields, $B_1^{lm}(t,r)$ and $B_3^{lm}(t,r)$, obeys [51]

$$\partial_t{}^2\tilde{B}_1^{lm}(t,r) = \partial_r^2\tilde{B}_1^{lm}(t,r) - \frac{l(l+1)}{r^2}\tilde{B}_1^{lm}(t,r) - 4\pi l(l+1)J_3^{lm}(t,r), \tag{3}$$

$$\partial_t{}^2 B_3^{lm}(t,r) = \partial_r^2 B_3^{lm}(t,r) - \frac{l(l+1)}{r^2}B_3^{lm}(t,r) - 4\pi\left[J_1^{lm}(t,r) - \partial_r\left(J_2^{lm}(t,r)\right)\right], \tag{4}$$

where

$$\tilde{B}_1^{lm}(t,r) = r^2 B_1^{lm}(t,r), \tag{5}$$

and $J_i^{lm}$ $(i = 1, 2, 3)$ are the vector spherical harmonics expansions of the current term. Using the condition $\mathrm{div}\vec{B} = 0$, $B_2^{lm}(t, r)$ is related to $B_1^{lm}(t, r)$ as

$$B_2^{lm}(t, r) = \frac{1}{l(l+1)} \partial_r \tilde{B}_1^{lm}(t, r). \tag{6}$$

Using the Ampére–Maxwell law, the evolution equation for the electric field is written as

$$\partial_t E_1^{lm}(t, r) = -\frac{l(l+1)}{r^2} B_3^{lm}(t, r) - 4\pi J_1^{lm}(t, r), \tag{7}$$

$$\partial_t E_2^{lm}(t, r) = -\partial_r \left( B_3^{lm}(t, r) \right) - 4\pi J_2^{lm}(t, r), \tag{8}$$

$$\partial_t E_3^{lm}(t, r) = \frac{1}{l(l+1)} \partial_t{}^2 \tilde{B}_1^{lm}(t, r). \tag{9}$$

The current term of a magnetic dipole moment is written as [52]

$$J^{\mu}(x) = -\nabla_{\lambda} \int d\tau \, m^{\lambda\mu} \frac{\delta^{(4)}(x^{\nu} - x_{\mathrm{s}}^{\nu}(\tau))}{\sqrt{-g}}, \tag{10}$$

where $m^{\lambda\mu}$ is a magnetization tensor, $\nabla_{\lambda}$ is a covariant derivative, $x_{\mathrm{s}}^{\nu}(\tau)$ is the position of the magnetic dipole moment, $\tau$ is its proper time, $\delta^{(4)}(x^{\mu})$ is a delta function in four dimensions, and $g$ is the determinant of the metric $g_{\mu\nu}$. We assume that the magnetic dipole vector is parallel to the angular momentum vector of the orbital motion. In spherical polar coordinates, the position of the NS, $x_{\mathrm{s}}^{\mu}(\tau)$, is written as

$$x_{\mathrm{s}}^{\mu}(\tau) = \left( t(\tau), a, \frac{\pi}{2}, \Omega t(\tau) \right). \tag{11}$$

Then, each component of the magnetization tensor $m^{\lambda\mu}$ is related to the $z$-component of the magnetic dipole moment $m^z$ as

$$m_{tr} = -m_{rt} = m^z r \Omega \dot{t}_{\mathrm{NS}}, \tag{12}$$

$$m_{r\phi} = -m_{\phi r} = m^z r \dot{t}_{\mathrm{NS}}, \tag{13}$$

$$m_{ij} = 0 \qquad \text{(others)}, \tag{14}$$

where the dot denotes the derivative with respect to the proper time $\tau$. Here, we used $m_{\mu\nu} = \dot{x}_s^{\rho}(\tau) \epsilon_{\rho\mu\nu\sigma} m^{\sigma}$, where $m^{\sigma}$ is the magnetic dipole moment vector and $\epsilon_{\mu\nu\sigma\rho}$ is the antisymmetric tensor in four dimensions. In this context, the source term of Eq. (10) is expanded in vector spherical harmonics as:

$$J_1^{lm}(t, r) = \frac{m^z}{|\dot{t}|^2} \frac{im}{a^3} Y_{lm}^* \left( \frac{\pi}{2}, \Omega t \right) \delta(r - a), \tag{15}$$

$$J_2^{lm}(t, r) = \frac{m^z im}{l(l+1)} Y_{lm}^* \left( \frac{\pi}{2}, \Omega t \right) \partial_r \left[ \frac{1}{r} \delta(r - a) \right], \tag{16}$$

$$J_3^{lm}(t, r) = -\frac{m^z}{l(l+1)} \partial_{\theta} Y_{lm}^* \left( \frac{\pi}{2}, \Omega t \right) \partial_r \left[ \frac{1}{r} \delta(r - a) \right], \tag{17}$$

where we used $\dot{t} = \left(1 - a^2 \Omega^2\right)^{-1/2}$.

We use Fourier transformation to solve the Maxwell equations. The Fourier transformation of the time-dependent equations of the magnetic field, Eqs. (3) and (4), is

$$\partial_r^2 B^{lm}(\omega,r) + \left(\omega^2 - \frac{l(l+1)}{r^2}\right) B^{lm}(\omega,r) = S^{lm}(\omega,r), \tag{18}$$

where $B^{lm}(\omega,r)$ is the Fourier transformation of $\tilde{B}_1^{lm}(t,r)$ or $B_3^{lm}(t,r)$, and $S^{lm}(\omega,r)$ is the Fourier transformation of $4\pi l(l+1)J_3^{lm}(t,r)$ or $4\pi\left[J_1^{lm}(t,r) - \partial_r\left(J_2^{lm}(t,r)\right)\right]$, respectively. We note that for $m=0$, $\omega=0$ in Eq. (18). Equation (18) is a Sturm–Liouville equation and we can solve it by imposing appropriate boundary conditions and constructing Green's functions.

To solve Eq. (18), we impose the boundary condition that the magnetic field is outgoing at infinity and regular at the origin for $m \neq 0$ modes, and the magnetic field is regular at infinity and at the origin for $m=0$ modes. For $m \neq 0$, a homogeneous solution of Eq. (18) with the outgoing boundary condition at infinity is $\omega r h_l^{(1)}(\omega r)$, and one with the regular boundary condition at the origin is $\omega r j_l(\omega r)$. Here, $j_l(x)$ is the spherical Bessel function of the first kind, and $h_l^{(1)}$ is the spherical Hankel function of the first kind. With these homogeneous solutions, we obtain the Green's function of Eq. (18), $G_{\omega,l}(r,r')$, for each frequency $\omega$ ($\neq 0$) as

$$G_{\omega,l}(r,r') = \begin{cases} -ir'\, h_l^{(1)}(\omega r') \cdot \omega r\, j_l(\omega r) & (r < r'), \\ -ir'\, j_l(\omega r') \cdot \omega r\, h_l^{(1)}(\omega r) & (r > r'). \end{cases} \tag{19}$$

For $m=0$, a homogeneous solution with the regular boundary condition at infinity is $r^{-l}$, and one with the regular boundary condition at the origin is $r^{l+1}$. Thus, the Green's function for $m=0$ modes is

$$G_{\omega,l}(r,r') = \begin{cases} -\frac{r'}{2l+1}\left(\frac{r}{r'}\right)^{l+1} & (r < r'), \\ -\frac{r'}{2l+1}\left(\frac{r'}{r}\right)^{l} & (r > r'). \end{cases} \tag{20}$$

We do not consider any effect of the companion on the electromagnetic field. If the companion is a BH, we need to impose a boundary condition such that the electromagnetic field is ingoing on the event horizon of the BH. If the companion is an NS, we need to impose some boundary condition for the magnetic field on the surface of the NS. In this paper we ignore such effects.

With these Green's functions, we derive $B_1^{lm}(\omega,r)$ and $B_3^{lm}(\omega,r)$ in Fourier space as

$$\begin{aligned} B_1^{lm}(\omega,r) = -i\frac{4\pi m^z}{r^2} Y^*_{lm,\theta}\left(\frac{\pi}{2},0\right)\delta(\omega - m\Omega)\Bigg\{ & \theta(r-a)\left[\frac{1}{r'}\partial_{r'}\left(r' j_l(\omega r')\right)\right]_{r'=a} \\ & \times\ \omega r h_l^{(1)}(\omega r) + \theta(a-r)\left[\frac{1}{r'}\partial_{r'}\left(r'\, h_l^{(1)}(\omega r')\right)\right]_{r'=a} \omega r j_l(\omega r)\Bigg\}, \end{aligned} \tag{21}$$

$$\begin{aligned} B_3^{lm}(\omega,r) = & -4\pi m^z m\Omega^2 Y^*_{lm}\left(\frac{\pi}{2},0\right)\delta(\omega - m\Omega) \\ & \times \Bigg\{\theta(r-a)\left(1 - \frac{m^2}{l(l+1)}\right) j_l(\omega a)\omega r h_l^{(1)}(\omega r) \\ & + \theta(a-r)\left(1 - \frac{m^2}{l(l+1)}\right) h_l^{(1)}(\omega a)\omega r j_l(\omega r) + \frac{i}{a\Omega^2 l(l+1)}\delta(r-a)\Bigg\} \end{aligned} \tag{22}$$

for $m \neq 0$ modes. For $m=0$ modes, the solutions are

$$B_1^{l0}(\omega,r) = 4\pi m^z \frac{1}{ar^2} Y^*_{l0,\theta}\delta(\omega)\left(\frac{\pi}{2},0\right)\left\{\theta(a-r)\frac{l}{2l+1}\left(\frac{r}{a}\right)^{l+1}\right.$$

$$- \theta(r-a)\frac{l+1}{2l+1}\left(\frac{a}{r}\right)^l\Bigg\}, \tag{23}$$

$$B_3^{l0}(\omega, r) = 0. \tag{24}$$

For $m \neq 0$ modes, by inverse Fourier transformation of the solution with Eq. (6), we obtain the electromagnetic field in terms of the vector spherical harmonics expansion as:

$$\begin{aligned} B_1^{lm}(t,r) = &-i\frac{4\pi m^z}{r^2}Y^*_{lm,\theta}\left(\frac{\pi}{2},0\right)e^{-im\Omega t} \\ &\times\Bigg\{\theta(r-a)\left[\frac{1}{r'}\partial_{r'}\left(r' j_l(m\Omega r')\right)\right]_{r'=a} m\Omega r h_l^{(1)}(m\Omega r) \\ &+\theta(a-r)\left[\frac{1}{r'}\partial_{r'}\left(r' h_l^{(1)}(m\Omega a')\right)\right]_{r'=a} m\Omega r j_l(m\Omega r)\Bigg\}, \end{aligned} \tag{25}$$

$$\begin{aligned} B_2^{lm}(t,r) = &-i\frac{4\pi m^z}{l(l+1)}Y^*_{lm,\theta}\left(\frac{\pi}{2},0\right)e^{-im\Omega t} \\ &\times\Bigg\{\theta(r-a)\left[\frac{1}{r'}\partial_{r'}\left(r' j_l(m\Omega r')\right)\right]_{r'=a}\frac{d}{dr}\left[m\Omega r h_l^{(1)}(m\Omega r)\right] \\ &+\theta(a-r)\left[\frac{1}{r'}\partial_{r'}\left(r' h_l^{(1)}(m\Omega r')\right)\right]_{r'=a}\frac{d}{dr}\left[m\Omega r j_l(m\Omega r)\right] - \frac{i}{r}\delta(r-a)\Bigg\}, \end{aligned} \tag{26}$$

$$\begin{aligned} B_3^{lm}(t,r) = &-4\pi m^z m\Omega^2 Y^*_{lm}\left(\frac{\pi}{2},0\right)e^{-im\Omega t}\Bigg\{\theta(r-a)\left(1-\frac{m^2}{l(l+1)}\right) \\ &\times j_l(m\Omega a) m\Omega r h_l^{(1)}(m\Omega r) + \theta(a-r)\left(1-\frac{m^2}{l(l+1)}\right)h_l^{(1)}(m\Omega a) m\Omega r j_l(m\Omega r) \\ &+\frac{i}{a\Omega^2 l(l+1)}\delta(r-a)\Bigg\}, \end{aligned} \tag{27}$$

where $\theta(x)$ is a step function. Using this magnetic field and Eqs. (7)–(9), we obtain the electric field as:

$$\begin{aligned} E_1^{lm}(t,r) = &\frac{4\pi i m^z l(l+1)}{r^2}\Omega Y^*_{lm}\left(\frac{\pi}{2},0\right)e^{-im\Omega t} \\ &\times\Bigg\{\theta(r-a)\left(1-\frac{m^2}{l(l+1)}\right)j_l(m\Omega a) m\Omega r h_l^{(1)}(m\Omega r) \\ &+\theta(a-r)\left(1-\frac{m^2}{l(l+1)}\right)h_l^{(1)}(m\Omega a) m\Omega r j_l(m\Omega r) + \frac{ia^3}{l(l+1)}\delta(r-a)\Bigg\}, \end{aligned} \tag{28}$$

$$\begin{aligned} E_2^{lm}(t,r) = &\,4\pi i m^z \Omega Y^*_{lm}\left(\frac{\pi}{2},0\right)e^{-im\Omega t} \\ &\times\Bigg\{\theta(r-a)\left(1-\frac{m^2}{l(l+1)}\right)j_l(m\Omega a)\frac{d}{dr}\left[m\Omega r h_l^{(1)}(m\Omega r)\right] \\ &+\theta(a-r)\left(1-\frac{m^2}{l(l+1)}\right)h_l^{(1)}(m\Omega a)\frac{d}{dr}\left[m\Omega r j_l(m\Omega r)\right]\Bigg\} \end{aligned} \tag{29}$$

$$E_3^{lm}(t,r) = -\frac{4\pi m^z m\Omega}{l(l+1)}Y^*_{lm,\theta}\left(\frac{\pi}{2},0\right)e^{-im\Omega t}\left\{\theta(r-a)\left[\frac{1}{r'}\partial_{r'}\left(r' j_l(m\Omega r')\right)\right]_{r'=a}\right.$$

$$\times m\Omega r h_l^{(1)}(m\Omega r) + \theta(a-r)\left[\frac{1}{r'}\partial_{r'}\left(r' h_l^{(1)}(m\Omega r')\right)\right]_{r'=a} m\Omega r j_l(m\Omega r)\Bigg\}. \quad (30)$$

For $m = 0$ modes, we obtain the magnetic field as:

$$B_1^{l0}(r) = 4\pi m^z \frac{1}{a} Y^*_{l0,\theta}\left(\frac{\pi}{2}, 0\right)\left\{\theta(a-r)\frac{l}{2l+1}\left(\frac{r}{a}\right)^{l+1} - \theta(r-a)\frac{l+1}{2l+1}\left(\frac{a}{r}\right)^{l}\right\}, \quad (31)$$

$$B_2^{l0}(r) = 4\pi m^z \frac{1}{a} Y^*_{l0,\theta}\left(\frac{\pi}{2}, 0\right)\left\{\theta(a-r)\frac{1}{2l+1}\left(\frac{r}{a}\right)^{l}\frac{1}{a} + \theta(r-a)\frac{1}{2l+1}\left(\frac{a}{r}\right)^{l+1}\frac{1}{a} - \delta(r-a)\right\}, \quad (32)$$

$$B_3^{l0}(r) = 0. \quad (33)$$

We note that the electric field does not contain the $m = 0$ modes because they are static modes and the electric field is induced only by the orbital motion of the magnetic dipole moment.

### 2.2. *Magnetic field configuration*

In this subsection we display the configuration of the magnetic field derived in the previous subsection and illustrate the importance of the higher multipole modes. With this configuration, we indicate the location in which the magnetic reconnection could occur in the late inspiral phase if plasma exists. We note that the magnetic reconnection process is associated with the motion of the plasma in the magnetosphere, and thus force-free or particle-in-cell simulations are needed for a more realistic description.

Figures 1 and 2 show the magnetic field configuration and the energy density of the electromagnetic field for a BH–NS binary just before the merger for the $z = 0.5M$ surface and $y = 0$ surface, respectively. Here, the NS is located at $(6M, 0, 0)$. It is found that there is a spiral arm in which the energy density of the electromagnetic field is significantly enhanced. As we will see below, this configuration is due to the superposition of several multipole modes. In the spiral arm, the poloidal magnetic field often changes its direction (see Fig. 3). In the presence of the plasma, the magnetic reconnection could occur in the region where the magnetic field direction changes steeply. In the spiral arm (for example, $(x, z) \sim (-35M, 0)$–$(-50M, 0)$ in Fig. 2) in particular, magnetic reconnection could occur. This speculation is confirmed by force-free simulation [44].

Figure 4 shows the energy density of the electromagnetic field at $\left(r_{\rm NS}/\sqrt{2}, 0, r_{\rm NS}/\sqrt{2}\right)$, where $r_{\rm NS} = \sqrt{(x-6M)^2 + y^2 + z^2}$ is the distance measured from the NS. The field strength is inversely proportional to $r$ on average for $r \gg R$, and the waveform does not have a sine-wave shape. This wave pattern is formed because of the dominant contribution to the field strength from not only the dipole mode but also the higher multipole modes. In the case of gravitational waves from binary compact stars, the $l = m = 2$ mode is dominant and the waveform has a sine-wave shape. However, the wave form of the electromagnetic wave is different from that of the gravitational wave. Due to the higher multipole modes of the electromagnetic field, sharp energy density peaks appear corresponding to the position of the spiral arm shown in Fig. 1. In the next subsection we show that the contribution of the higher $l, m$ modes enhances the Poynting flux.

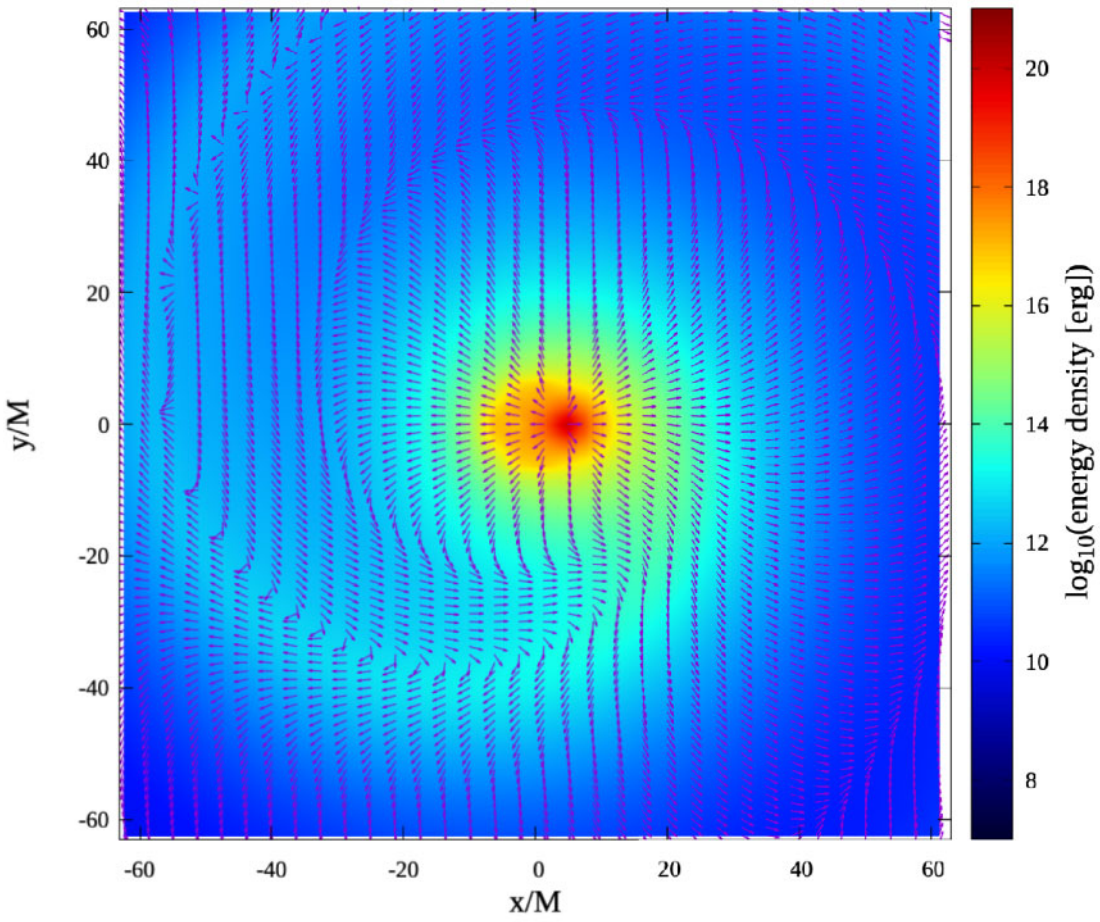


**Fig. 1.** The magnetic-field configuration for the $z = 0.5M$ surface. The color shows the strength of the energy density in a logarithmic scale, $\log_{10}\left(\frac{1}{8\pi}(B^2 + E^2)\right)$, and the arrows show the direction of the magnetic field. The NS is located at $(x, y, z) = (6M, 0, 0)$ and orbiting according to Kepler's law. The center of mass is at the origin, and the magnetic field at the pole of the NS is set to be equal to $10^{12}$ G. We sum higher multipole terms up to $l = 85$ modes. We can see the spiral arm configuration, for which the energy density is high, and near the spiral arm the magnetic field direction changes steeply. The convergence of the multipole expansion is poor near $x^2 + y^2 + (0.5M)^2 \sim (6M)^2$, so we interpolate the magnetic field there.

### 2.3. *Luminosity and special relativistic correction*

In terms of $B_i^{lm}$ and $E_i^{lm}$ $(i = 1, 2, 3)$, the Poynting flux at infinity is written as

$$
\begin{aligned}
L_{\rm EM} &= \int d\vec{S} \cdot \left( \frac{1}{4\pi} \vec{E} \times \vec{B} \right) \\
&= \int \frac{d\Omega}{4\pi} \sum_{lm\, l'm'} \Big[ Y_{lm,\theta} Y_{l'm',\theta} \left( E_2^{lm} B_3^{l'm'} - B_2^{lm} E_3^{l'm'} \right) \\
&\quad + \frac{1}{\sin^2\theta} Y_{lm,\phi} Y_{l'm',\phi} \left( -E_3^{lm} B_2^{l'm'} + E_2^{lm} B_3^{l'm'} \right) \\
&\quad + \frac{1}{\sin\theta} Y_{lm,\theta} Y_{l'm',\phi} \left( E_2^{lm} B_2^{l'm'} - B_2^{lm} E_2^{l'm'} + E_3^{llm} B_3^{l'm'} - B_3^{lm} E_3^{l'm'} \right) \Big]
\end{aligned}
$$

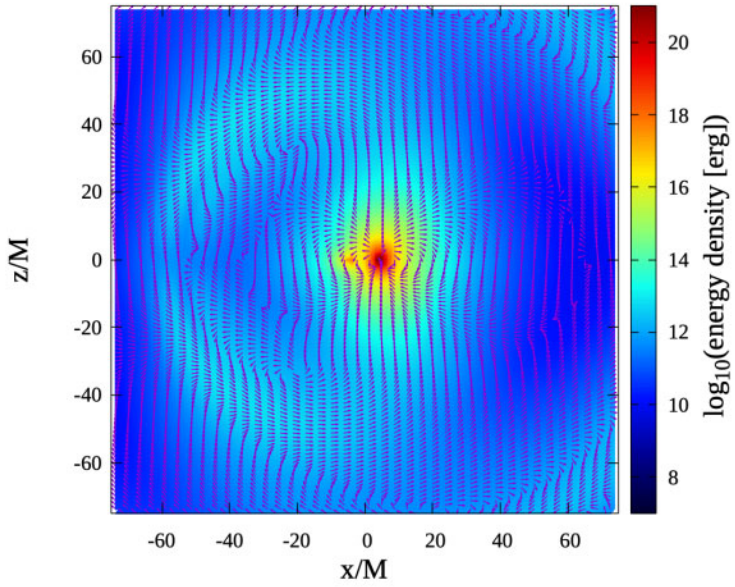


**Fig. 2.** As Fig. 1 but for the $y = 0$ surface. Near the NS the magnetic field is dipolar, and near the spiral arm the magnetic field direction changes steeply (displayed in Fig. 1; see also Fig. 3). This region is a candidate for magnetic reconnection in the presence of plasma.

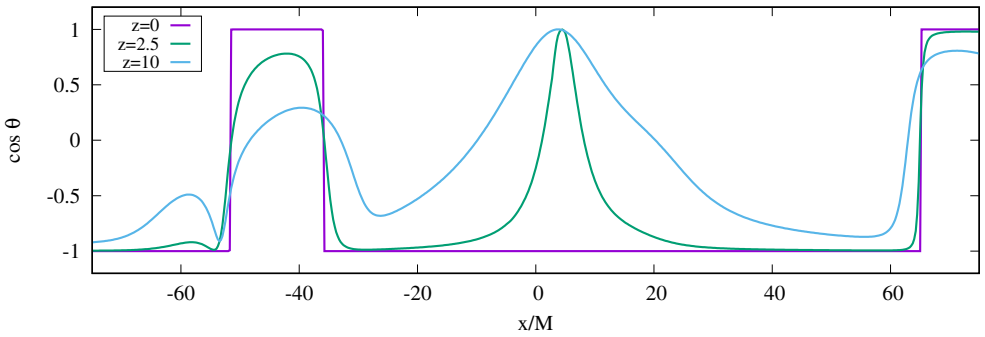


**Fig. 3.** The cosine of the angle between the $z$-axis and the magnetic field in $(y, z) = (0, 0)$ (purple line), $(y, z) = (0, 2.5M)$ (green line), and $(y, z) = (0, 10M)$ (blue line). Here, $\cos\theta = \vec{B} \cdot \vec{e}_z/|\vec{B}|$, where $\vec{e}_z$ is the unit vector in the $z$ direction. Near $x/M \sim -35$, $x/M \sim -50$, and $x/M \sim 65$, the magnetic field direction changes steeply.

$$= \frac{1}{4\pi} \sum_{l\,m} (-1)^m \, l(l+1) \left( E_2^{lm} B_3^{l\,-m} - B_2^{lm} E_3^{l\,-m} \right). \tag{34}$$

Considering the asymptotic form of the spherical Hankel functions of the first kind at infinity, $h_l^{(1)}(x) \to \exp\left(i(x - \pi(l+1)/2)\right)/x$, we obtain an analytic formula for the luminosity as

$$L_{\rm EM} = \frac{4(m^z)^2\Omega^6 a^2}{15} \frac{15\pi}{a^2\Omega^2} \sum_{lm} l(l+1) \left[ m^2 \left| Y_{lm}\left(\frac{\pi}{2}, 0\right) \right|^2 \left(1 - \frac{m^2}{l(l+1)}\right)^2 \left(j_l\left(m\Omega a\right)\right)^2 \right.$$
$$\left. + \frac{m^4}{l^2(l+1)^2} \left| Y_{lm,\theta}\left(\frac{\pi}{2}, 0\right) \right|^2 \left( \frac{j_l\left(m\Omega a\right)}{m\Omega a} + j_l'\left(m\Omega a\right) \right)^2 \right], \tag{35}$$

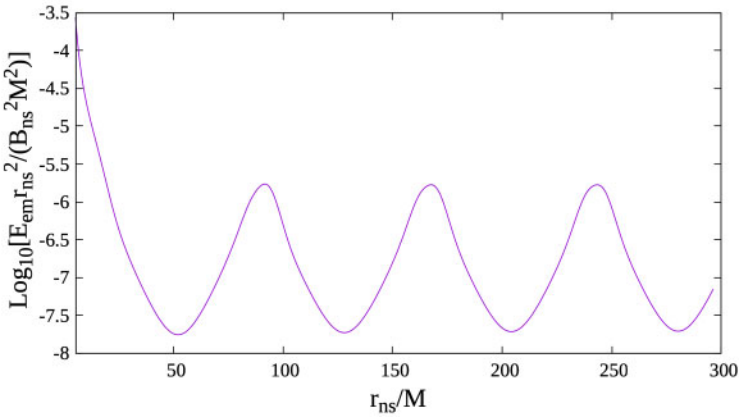


**Fig. 4.** The energy density times radius squared, $\frac{1}{8\pi}(E^2+B^2)r_{\rm NS}^2$, in a logarithmic scale at $(r_{\rm NS}/\sqrt{2}, 0, r_{\rm NS}/\sqrt{2})$. The left edge of the $r$-axis is at the point where the NS exists. Near the NS the magnetic field is dipolar and the energy density is proportional to $r^{-6}$. For $r > c/\Omega + a = 22M$, the electromagnetic field is composed primarily of electromagnetic waves and the energy density is proportional to $r^{-2}$ on average. We see one peak at each spiral arm due to the summation of the multiple modes.

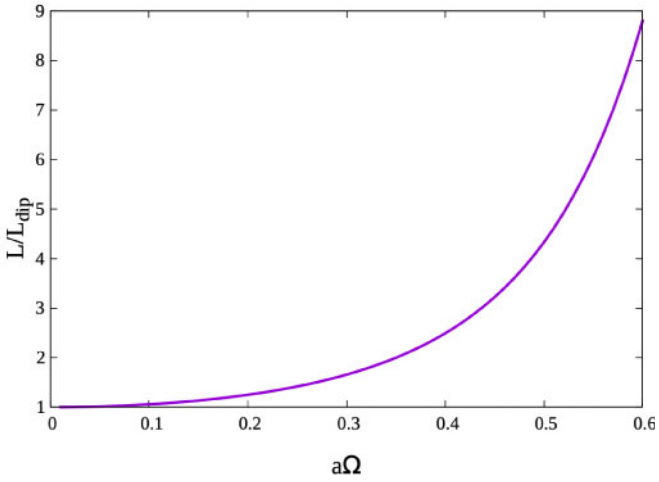


**Fig. 5.** The special relativistic correction for the luminosity, calculated by the analytic formula in Eq. (35). At the ISCO of a Schwarzschild BH, the orbital velocity is $a\Omega = \sqrt{M_{\rm BH}/6M} < 0.41$. Therefore, the special relativistic correction would be less than 2.6.

where $j_l'(x) = dj_l(x)/dx$. The first term, $\frac{4(m^z)^2\Omega^6a^2}{15}$, agrees with the luminosity of the dipole radiation derived in Ref. [21], and the remaining terms correspond to the special relativistic correction to the radiation formula due to the higher multipole modes of the electromagnetic field. Figure 5 shows the special relativistic correction of this analytic luminosity. We suppose that the quasi-circular orbit of the binary terminates at an ISCO around a Schwarzschild BH. In the following discussion, we set the radius of the ISCO to be approximately $r\ (= aM/M_{\rm BH}) = 6M_{\rm BH}$. At the ISCO of the BH, the velocity $a\Omega$ of the NS is $\sqrt{M_{\rm BH}/6M}$, and the special relativistic correction is less than 2.6. The luminosity is enhanced by the higher multipole modes, and this enhancement is unique to electromagnetic waves. In the case of gravitational waves from compact binaries, the higher multipole modes reduce the luminosity.

We expand Eq. (35) in terms of $a\Omega$, perform the summation with respect to $l, m$, and obtain $L_{\rm EM}$ in a series of the velocity $v = a\Omega$ as

$$L_{\rm EM} = \frac{4(m^z)^2\Omega^6 a^2}{15}\left[1 + \frac{11v^2}{2} + 16v^4 + 35v^6 + 65v^8 + \frac{217v^{10}}{2} + 168v^{12} + 246v^{14} + 345v^{16} + \frac{935v^{18}}{2} + 616v^{20} + O\left((a\Omega)^{22}\right)\right]. \tag{36}$$

Each $l, m$ mode contributes substantially to the luminosity. To reveal this contribution we write the luminosity as

$$L_{\rm EM} = \frac{4(m^z)^2\Omega^6 a^2}{15}\sum_{l,m}\eta_{l,m}, \tag{37}$$

where $\eta_{l,m}$ is the Poynting flux of the $l, m$ mode divided by the luminosity at the zeroth order, $4(m^z)^2\Omega^6 a^2/15$, and it expresses the contribution of the $l, m$ mode in the Poynting flux. We show $\eta_{l,m}$ only for $m > 0$ because $\eta_{l,m} = \eta_{l,-m}$:

$$\eta_{1,1} = \frac{5}{16} - \frac{v^2}{16} + \frac{3v^4}{560} - \frac{v^6}{3780} + \frac{v^8}{116424} - \frac{v^{10}}{5045040} + \frac{v^{12}}{291891600} - \frac{v^{14}}{21709437750} + \frac{v^{16}}{2016565551000} - \frac{v^{18}}{228678533483400} + \frac{v^{20}}{31079491596153000} + O\left(v^{22}\right), \tag{38}$$

$$\eta_{2,1} = \frac{3}{16} - \frac{5v^2}{112} + \frac{31v^4}{7056} - \frac{v^6}{4158} + \frac{115v^8}{13621608} - \frac{47v^{10}}{227026800} + \frac{41v^{12}}{10916745840} - \frac{v^{14}}{19037506950} + \frac{193v^{16}}{330313437253800} - \frac{v^{18}}{188806378927320} + \frac{31v^{20}}{776987289903825000} + O\left(v^{22}\right), \tag{39}$$

$$\eta_{2,2} = \frac{4v^2}{3} - \frac{16v^4}{21} + \frac{256v^6}{1323} - \frac{1280v^8}{43659} + \frac{5120v^{10}}{1702701} - \frac{4096v^{12}}{18243225} + \frac{131072v^{14}}{10234449225} - \frac{262144v^{16}}{453727248975} + \frac{524288v^{18}}{24773507794035} - \frac{2097152v^{20}}{3263346617596065} + O\left(v^{22}\right), \tag{40}$$

$$\eta_{3,1} = \frac{121v^4}{26880} - \frac{121v^6}{241920} + \frac{11v^8}{435456} - \frac{11v^{10}}{14152320} + \frac{v^{12}}{60652800} - \frac{v^{14}}{3866616000} + \frac{v^{16}}{318351384000} - \frac{v^{18}}{32758357413600} + \frac{11v^{20}}{45206533230768000} + O\left(v^{22}\right), \tag{41}$$

$$\eta_{3,2} = \frac{32v^2}{21} - \frac{64v^4}{63} + \frac{608v^6}{2079} - \frac{3968v^8}{81081} + \frac{72704v^{10}}{13378365} - \frac{210944v^{12}}{487354725} + \frac{9404416v^{14}}{361129851225} - \frac{5636096v^{16}}{4587686628525} + \frac{133169152v^{18}}{2848953396314025} - \frac{85458944v^{20}}{58274046742786875} + O\left(v^{22}\right), \tag{42}$$

$$\eta_{3,3} = \frac{6561v^4}{1792} - \frac{6561v^6}{1792} + \frac{32805v^8}{19712} - \frac{59049v^{10}}{128128} + \frac{177147v^{12}}{2013440} - \frac{531441v^{14}}{42785600} + \frac{14348907v^{16}}{10568043200} - \frac{43046721v^{18}}{362483881760} + \frac{129140163v^{20}}{15158416873600} + O\left(v^{22}\right), \tag{43}$$

$$\eta_{4,1} = \frac{5\nu^4}{37632} - \frac{\nu^6}{59136} + \frac{283\nu^8}{295975680} - \frac{43\nu^{10}}{1331890560} + \frac{311\nu^{12}}{420496876800} - \frac{173\nu^{14}}{13981521153600} + \frac{233\nu^{16}}{1468059721128000} - \frac{191\nu^{18}}{118178807550804000} + \frac{\nu^{20}}{74546928696240000} + O\left(\nu^{22}\right), \quad (44)$$

$$\eta_{4,2} = \frac{512\nu^6}{6615} - \frac{2048\nu^8}{72765} + \frac{16384\nu^{10}}{3468465} - \frac{32768\nu^{12}}{66891825} + \frac{524288\nu^{14}}{14783093325} - \frac{2097152\nu^{16}}{1092306340125} + \frac{16777216\nu^{18}}{206445898283625} - \frac{8388608\nu^{20}}{3021617238514875} + O\left(\nu^{22}\right), \quad (45)$$

$$\eta_{4,3} = \frac{10935\nu^4}{1792} - \frac{19683\nu^6}{2816} + \frac{50132601\nu^8}{14094080} - \frac{7617321\nu^{10}}{7047040} + \frac{495834453\nu^{12}}{2224851200} - \frac{2482360911\nu^{14}}{73976302400} + \frac{10029885993\nu^{16}}{2589170584000} - \frac{73997313399\nu^{18}}{208428232012000} + \frac{3486784401\nu^{20}}{131476064720000} + O\left(\nu^{22}\right), \quad (46)$$

$$\eta_{4,4} = \frac{8192\nu^6}{945} - \frac{131072\nu^8}{10395} + \frac{4194304\nu^{10}}{495495} - \frac{33554432\nu^{12}}{9555975} + \frac{2147483648\nu^{14}}{2111870475} - \frac{34359738368\nu^{16}}{156043762875} + \frac{1099511627776\nu^{18}}{29492271183375} - \frac{2199023255552\nu^{20}}{431659605502125} + O\left(\nu^{22}\right), \quad (47)$$

$$\eta_{5,1} = \frac{841\nu^8}{670602240} - \frac{841\nu^{10}}{8717829120} + \frac{841\nu^{12}}{242853811200} - \frac{841\nu^{14}}{10837351324800} + \frac{841\nu^{16}}{686365583904000} - \frac{841\nu^{18}}{57654709047936000} + \frac{841\nu^{20}}{6148088519384448000} + O\left(\nu^{22}\right), \quad (48)$$

$$\eta_{5,2} = \frac{64\nu^6}{10395} - \frac{1024\nu^8}{405405} + \frac{7424\nu^{10}}{15810795} - \frac{19456\nu^{12}}{366522975} + \frac{950272\nu^{14}}{229809905325} - \frac{16384\nu^{16}}{68746552875} + \frac{4784128\nu^{18}}{449278364910375} - \frac{34340864\nu^{20}}{90059890420670625} + O\left(\nu^{22}\right), \quad (49)$$

$$\eta_{5,3} = \frac{45927\nu^8}{112640} - \frac{413343\nu^{10}}{1464320} + \frac{8680203\nu^{12}}{95180800} - \frac{3720087\nu^{14}}{202259200} + \frac{100442349\nu^{16}}{38429248000} - \frac{43046721\nu^{18}}{153716992000} + \frac{129140163\nu^{20}}{5463940352000} + O\left(\nu^{22}\right), \quad (50)$$

$$\eta_{5,4} = \frac{65536\nu^6}{3465} - \frac{4194304\nu^8}{135135} + \frac{121634816\nu^{10}}{5270265} - \frac{1275068416\nu^{12}}{122174325} + \frac{249108103168\nu^{14}}{76603301775} - \frac{17179869184\nu^{16}}{22915517625} + \frac{20066087206912\nu^{18}}{149759454970125} - \frac{576144092954624\nu^{20}}{30019963473556875} + O\left(\nu^{22}\right), \quad (51)$$

$$\eta_{5,5} = \frac{244140625\nu^8}{12773376} - \frac{6103515625\nu^{10}}{166053888} + \frac{30517578125\nu^{12}}{925157376} - \frac{762939453125\nu^{14}}{41285147904} + \frac{3814697265625\nu^{16}}{522945206784} - \frac{95367431640625\nu^{18}}{43927397369856} + \frac{2384185791015625\nu^{20}}{4684257919531008} + O\left(\nu^{22}\right). \quad (52)$$

Figures 6 and 7 show the dependence of $\eta_{lm}$ on the velocity, $a\Omega$. The left panel of Fig. 6 shows the $l = 1, 2, 3$ modes, the right panel of Fig. 6 shows the $l = 4$ mode, and the left panel of Fig. 7 shows the $l = 5$ mode. It is found that for each $l$, the higher $m$ modes become dominant for higher velocity. The right panel of Fig. 7 shows the contribution of each $l$ mode (the summation of $m$ modes) for the

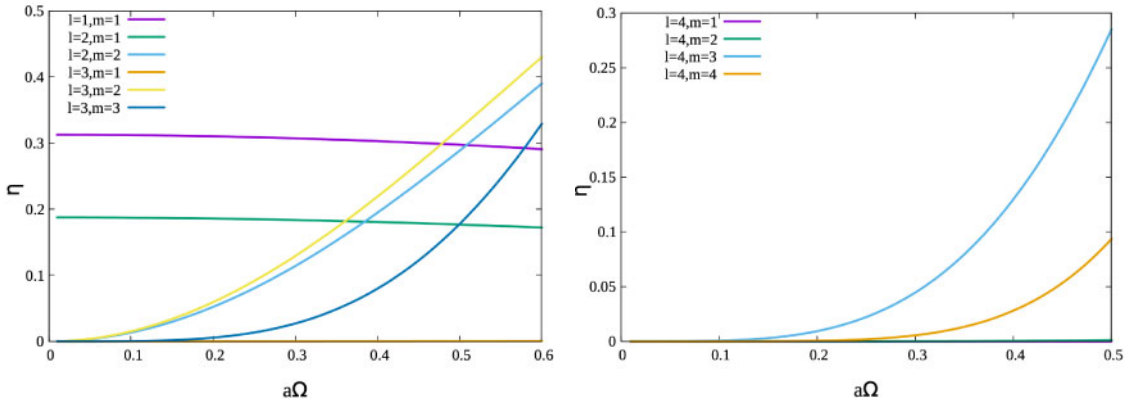


**Fig. 6.** The velocity dependence of $\eta_{lm}$. The left panel shows $l = 1, 2, 3$, and the right panel shows $l = 4$.

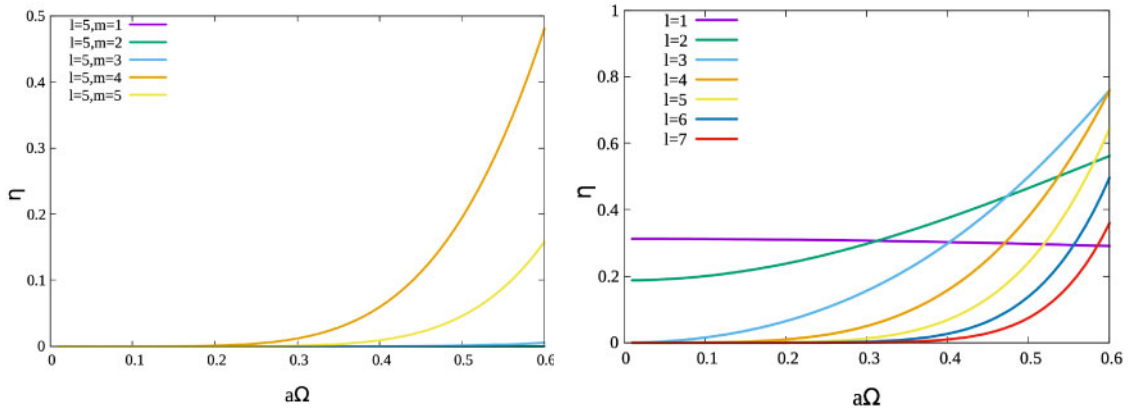


**Fig. 7.** The velocity dependence of $\eta_{lm}$ for $l = 5$ modes (left panel). The velocity dependence of $\sum_{m=1}^{l} = \eta_{lm}$ for $l = 1$–$7$ (right panel).

$l = 1$–$7$ modes. This figure indicates that the contribution of $l > 7$ modes would be subdominant in a few milliseconds before the merger.

At zeroth order of $v/c$, the luminosity is

$$L = \frac{4}{15c^5}\left(\frac{B_{\rm NS}R_{\rm NS}^3}{2}\right)^2 \Omega^6 a^2, \tag{53}$$

and, apart from the difference in the numerical coefficient and the dependence on the inclination angle, this is different from the dipole radiation formula for pulsars, $\sim B_{\rm NS}^2 R_{\rm NS}^6 \Omega^4/c^3$, by an additional factor of $(a\Omega/c)^2$. Here, we recover the speed of light, $c$, for clarification of the physical dimensions. This difference is understood as follows. The time-dependent part of the magnetic field is of the order of $B_{\text{t-dep}} \sim B_{\rm dip}\, a\Omega/c$, which is the difference between the dipole magnetic field and the Lorentz-boosted magnetic field. The wave field becomes comparable to the dipole field at $r \sim c/\Omega$. At these points, the energy density, $\varepsilon_{\rm mag}$, is

$$\varepsilon_{\rm mag} \sim \frac{1}{8\pi}\left(B_{\text{t-dep}}\left(\frac{R_{\rm NS}}{c/\Omega}\right)^3\right)^2. \tag{54}$$

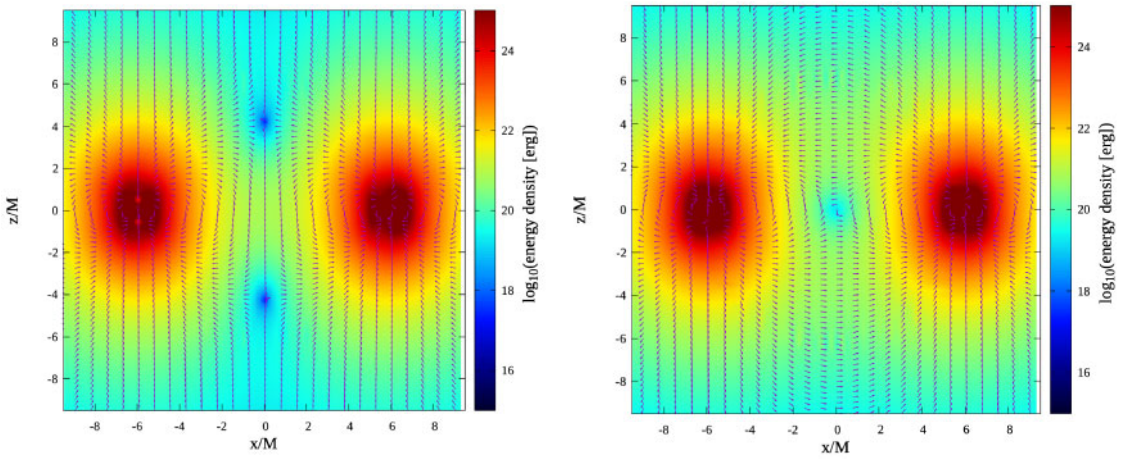


**Fig. 8.** The magnetic field configuration around a BNS. The left panel shows the magnetic field configuration of aligned magnetic dipole moments. The right panel shows that of anti-aligned ones. The convergence of multipole expansion is poor near $r \sim a$, so we interpolate the magnetic field there.

This energy density is radiated at the speed of light. Therefore, the order of the luminosity is

$$L \sim \varepsilon_{\rm mag} \times 4\pi \left(\frac{c}{\Omega}\right)^2 c \sim \frac{1}{2c^5} B_{\rm NS}^2 R_{\rm NS}^6 \Omega^6 a^2. \tag{55}$$

### *2.4. Electromagnetic field around a BNS*

Using the solution of the Maxwell equations in vacuum shown in Eqs. (25)–(33), we also calculate the electromagnetic field around BNSs in which the NSs have magnetic fields of comparable strength. For simplicity, we set that the NSs have the same magnetic field strength at their pole and have the same mass. The separation is set to be 50 km. We calculate two cases. In the first case, both NSs have aligned magnetic dipole moments. In the second case, both NSs have anti-aligned magnetic dipole moments. We consider the magnetic field profile, which is determined by the superposition of two different magnetic fields induced by each NS. One of the fields is calculated using Eqs. (25)–(33), which express the magnetic field induced by one of the NSs. In addition, due to the symmetry relative to the $z$-axis, the field contribution from the other NS can be calculated by transforming Eqs. (25)–(33) with a rotation relative to the $z$-axis by $\pi$.

Figure 8 shows the electromagnetic field around a BNS. The left panel of Fig. 8 shows the magnetic field configuration of aligned magnetic dipole moments. There are two regions around which the magnetic field is weaker. For this case, we simply have a double spiral arm structure and do not have noticeable differences from the single-NS case. The right panel of Fig. 8 shows the magnetic field configuration for the anti-aligned case. Near the origin, the magnetic field has the opposite direction (X-point) and magnetic reconnection could occur in the presence of plasma.

The resistive magnetohydrodynamic simulations for BNS in Refs. [31,32] show that, for the aligned case, the current sheets first arise far from the stars. This current sheet formation might be due to the spiral arm structure of the electromagnetic field. They also show that, for the anti-aligned case, the current sheet formation begins between the stars. The X-point in the anti-aligned case might trigger the current sheet formation between the stars.

## 3. Electromagnetic counterpart of late inspiraling neutron-star binaries

Recently, Ref. [44] showed that an orbiting NS generates a magnetosphere around the NS. In this section we first indicate that the electric field induced by the orbital motion is indeed likely to generate a magnetosphere. Then, we consider possible electromagnetic radiation as a precursor and evaluate whether the precursor is observable or not, with the assumption that the total electromagnetic flux is converted into any kind of electromagnetic radiation or particle wind like pulsars.

### *3.1. Magnetosphere formation*

For an isolated rotating NS (i.e. a pulsar), we assume that the NS is a rotating good conductor and the magnetic fields inside and outside the NS are dipole. Then, an electric field parallel to the dipole magnetic field lines is induced at the surface of the NS, and therefore a magnetosphere is generated [53]. The charge number density of the magnetosphere (Goldreich–Julian density) is given by Gauss's law under no electric field condition in the comoving frame of the plasma.

In this subsection we consider the magnetosphere induced by the orbital motion of the NS. If the outside of the NS is vacuum, the magnetic dipole moment of the NS accelerated in the orbital motion induces an electric field on the NS surface, and its component parallel to the magnetic field lines is likely to pull out the charged particles from the NS surface. The charged particles should be distributed to cancel the induced electric field in the plasma's comoving frame and create a magnetosphere. The most interesting feature of this magnetosphere is that it is induced by the orbital motion. Thus, the surface charge density may be different from that of an isolated pulsar and the electromagnetic field is not static (e.g. Ref. [44]). We can estimate the charge density of the magnetosphere in a similar way to an isolated pulsar. We assume that the plasma in the magnetosphere has a velocity, $\vec{v}$, in the center-of-mass frame, and then the plasma should be distributed to cancel the induced electric field in the plasma's comoving frame. Thus, the electric field in the center-of-mass frame is

$$\vec{E} = -\frac{\vec{v}}{c} \times \vec{B}. \tag{56}$$

Using Gauss's law, we can calculate the charge density in the center-of-mass frame as

$$\begin{aligned} \rho_{\rm c} &= \frac{1}{4\pi} \vec{\nabla} \cdot \vec{E} \\ &= \frac{1}{4\pi c} \left[ \left( \vec{\nabla} \times \vec{v} \right) \cdot \vec{B} - \left( \vec{\nabla} \times \vec{B} \right) \cdot \vec{v} \right]. \end{aligned} \tag{57}$$

In the magnetosphere of an isolated pulsar with a dipole magnetic field, the ratio of the second term to the first term is of order $(v_{\rm rot}/c)^2$, where $v_{\rm rot}$ is the rotation velocity of the plasma in the magnetosphere. This is because $\vec{\nabla} \times \vec{B} = 4\pi\rho_{\rm c}\vec{v}_{\rm rot}/c$ for the stationary pulsar case. Thus, near the surface, the second term could be neglected and the first term of Eq. (57) mainly contributes to the charge density of the magnetosphere. We note that in the pulsar case, the second term is proportional to $\rho_{\rm c}$ and $\rho_{\rm c} = 0$ if the first term vanishes. By contrast, for the binary case, $\vec{\nabla} \times \vec{B} \neq 4\pi\rho_{\rm c}\vec{v}_{\rm rot}/c$ in general due to the orbital motion (i.e. $\partial E/\partial t \neq 0$). Therefore, even if the NS is irrotating and the motion of the plasma is the same as that of the NS ($\vec{\nabla} \times \vec{v} = 0$), the second term of Eq. (57) contributes to inducing the charge density of the magnetosphere, leading to $\rho_{\rm c} \neq 0$.

We estimate the order of the charge number density of this magnetosphere. First, we separate the magnetic field into three parts,

$$\vec{B} = \vec{B}_{\rm dip} + \vec{B}_{\rm moving} + \vec{B}_{\rm rad}, \tag{58}$$

where $\vec{B}_{\rm dip}$, $\vec{B}_{\rm moving}$, and $\vec{B}_{\rm rad}$ denote the pure dipole magnetic field, the modification of the dipole magnetic field due to the orbital motion, and the radiative magnetic field, respectively. We note that $\vec{B}_{\rm moving} + \vec{B}_{\rm rad}$ is equal to $\vec{B}_{\rm t\text{-}dip}$. The first and second terms fall off as $r^{-3}$, and the last one as $r^{-1}$. The rotation of the total magnetic field is nonzero due to the second and third terms,

$$\vec{\nabla} \times \vec{B} = \vec{\nabla} \times \left( \vec{B}_{\rm moving} + \vec{B}_{\rm rad} \right) \neq \vec{0}. \tag{59}$$

Thus, even if the plasma is irrotating, i.e. $\vec{\nabla} \times \vec{v} = 0$, Eq. (57) gives $\rho_{\rm c} \neq 0$, that is, a magnetosphere is induced by the orbital motion. By considering the Lorentz transformation of the pure dipole magnetic field $B_{\rm dip}$ with velocity $v = a\Omega$, we can estimate the magnetic field strength induced by the orbital motion as $B_{\rm moving} \sim (a\Omega/c)\, B_{\rm dip}$. With the fact that the magnetic field changes in the length scale of the orbital separation, we estimate $\left|\vec{\nabla} \times \vec{B}\right| \sim B_{\rm moving}/a$, and then, using Eq. (57), the order of the charge density becomes

$$\rho_{\rm c} \sim -\frac{a\Omega}{4\pi c} \frac{v B_{\rm dip}}{ca} = -\frac{B_{\rm dip}\Omega}{2\pi c} \frac{a\Omega}{2c}. \tag{60}$$

This expression agrees broadly with the result of a force-free simulation in Ref. [44].

For the late inspiral phase, the angular velocity of the orbital motion would become much higher than that of the intrinsic spin, and $a\Omega$ becomes of the order of $0.1c$. Thus, the magnetosphere induced by the orbital motion becomes dominant even in the case of a spinning NS with spin period 0.1–1 s. The particle number density is estimated as

$$n \simeq 3.1 \times 10^{12}\,{\rm cm}^{-3} \left( \frac{B}{10^{12}\,{\rm G}} \right) \left( \frac{M_{\rm c}}{10\,M_\odot} \right) \left( \frac{a}{90\,{\rm km}} \right)^{-2}. \tag{61}$$

This is larger than the Goldreich–Julian density of a typical pulsar with a period $P = 1\,{\rm s}$, $n \sim 7 \times 10^{10}\,{\rm cm}^{-3}\, B_{12} P_0^{-1}$ (here, $B = 10^{12}\,{\rm G}\, B_{12}$ and $P = 1\,{\rm s}\, P_0$).

### 3.2. *Possible precursor radiation and its observability*

An accelerated magnetic dipole moment radiates electromagnetic waves as Poynting flux. In this subsection we evaluate the luminosity and the observability of precursors to BNS and BH–NS binary mergers. Some kinds of radiation from pulsars are comparable to the total Poynting flux that is estimated by the magnetic dipole emission (for a review, see Refs. [54–56]). In considering the observability, we assume that the radiation efficiency is approximately equal to that of pulsars suggested by observations [57–62].

First, we consider the luminosity of a BNS just before its merger. We set the mass of each NS as $1.4\,M_\odot$ and the separation as 30 km. Then, the orbital velocity of the NS is $0.19c$, and the special relativistic correction is $f_{\rm r} \sim 1.2$. Using Eq. (36), the luminosity is (see Fig. 9)

$$L_{\rm BNS} \simeq 5.8 \times 10^{40}\,{\rm erg\,s}^{-1} \left( \frac{f_{\rm r}}{1.2} \right) \left( \frac{B_{\rm NS}}{10^{12}\,{\rm G}} \right)^2 \left( \frac{R_{\rm NS}}{12\,{\rm km}} \right)^6 \left( \frac{M_{\rm NS}}{1.4\,M_\odot} \right)^3 \left( \frac{R}{30\,{\rm km}} \right)^{-7}. \tag{62}$$

Next, we consider the luminosity of a BH–NS binary in which the NS is at the ISCO of a Schwarzschild BH. We set the mass of the BH as $10\,M_\odot$ and the separation as 90 km (ISCO of

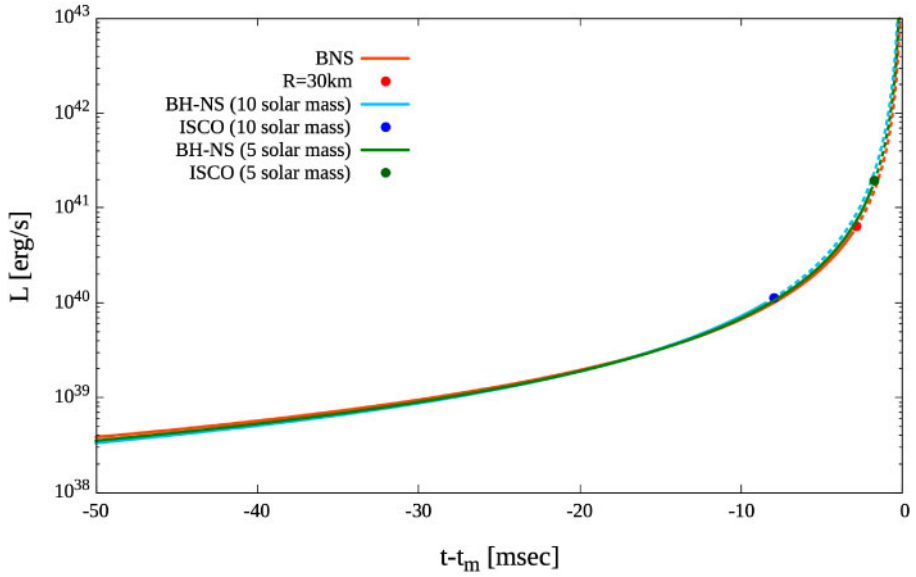


**Fig. 9.** Light curve of the total luminosity. Here, $t_{\rm m}$ denotes the merger time. We fix the magnetic field at the NS pole as $10^{12}$ G, the mass of the NS as $1.4\,M_\odot$, and the radius of the NS as 12 km. The BH mass is $10\,M_\odot$ and $5\,M_\odot$. We assume that the BNS merges when the separation reaches 30 km (red dot). We also assume that the BH–NS binary merges when the separation reaches 90 km for the $10\,M_\odot$ BH–NS binary case (blue dot), and 45 km for the $5\,M_\odot$ BH–NS binary case (green dot).

a Schwarzschild BH). The velocity of the NS is $0.38c$, and the special relativistic correction is $f_{\rm r} \sim 2.3$. Then the luminosity is (see Fig. 9)

$$L_{\rm NS-BH} \simeq 1.0 \times 10^{40}\,{\rm erg\,s^{-1}} \left(\frac{f_{\rm r}}{2.3}\right) \left(\frac{B_{\rm NS}}{10^{12}\,{\rm G}}\right)^2 \left(\frac{R_{\rm NS}}{12\,{\rm km}}\right)^6 \times \left(\frac{M_{\rm BH}}{10\,M_\odot}\right)^2 \left(\frac{M_{\rm BH}+M_{\rm NS}}{11.4\,M_\odot}\right) \left(\frac{R}{90\,{\rm km}}\right)^{-7}. \quad (63)$$

We note that the orbital radius of the ISCO of a BH depends on its spin. Thus, if we assume that the spin of the BH is parallel to the orbital angular momentum, the ISCO can be smaller than $6M_{\rm BH}$ down to $M_{\rm BH}$ and $L_{\rm NS-BH}$ reaches $\sim 10^{42}$ erg s$^{-1}$ at 1 ms before the merger.

In both cases, the luminosity just before the merger is typically $\sim 5 \times 10^{40}$ erg s$^{-1}$. Hereafter, we use this value as a typical value of the maximum luminosity. Also, since the event rate is approximately one BNS merger per year per 100 Mpc cubic volume [12], we set the luminosity distance as 100 Mpc, and evaluate the observability of the electromagnetic counterparts.

### *3.2.1. Radio wave emission*

We first explore the observability of the radio wave emission. According to the catalogue of Ref. [57], observed spinning-down pulsars emit radio waves with luminosity $\epsilon_{\rm r} \sim 10^{-6}$–$10^{-4}$ of its spin-down luminosity (Fig. 10). We note that this catalogue contains all types of pulsars except for accretion-powered systems. For example, the catalogue includes gamma-ray pulsars, which are quiet in radio [58–61]. Some fraction of the Poynting flux is radiated as strong coherent emission, such as the giant pulses of the Crab pulsar, and might also power fast radio bursts (FRBs) [63–65]. If a radio burst is radiated after the merger of an NS binary, the dynamical ejecta around the merger remnant

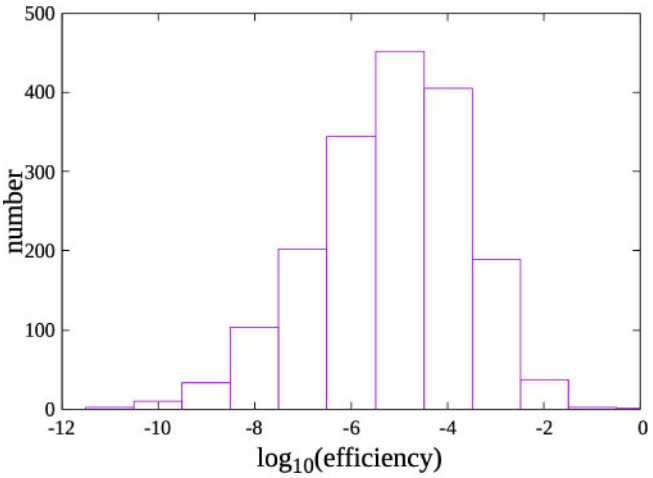


**Fig. 10.** The radio emission efficiency for pulsars from Ref. [57]. The efficiency is defined as the ratio of radio luminosity to spin-down luminosity. We use the radio luminosity at 1.4 GHz in the ATNF pulsar catalogue and assume that the radio luminosity is equal to $\nu L_\nu$.

shields the radio wave [66]. However, in the precursor case, only the plasma in the magnetosphere is relevant for shielding the radio wave.

If we assume that a fraction $\epsilon_{\rm r}$ of the total luminosity goes into radio emission, the spectral flux density at $\nu = 1.4\,{\rm GHz}$ is

$$F_\nu \simeq 0.5\,{\rm mJy}\left(\frac{L}{5\times10^{40}\,{\rm erg\,s^{-1}}}\right)\left(\frac{\epsilon_{\rm r}}{10^{-4}}\right)\left(\frac{D}{100\,{\rm Mpc}}\right)^{-2}\left(\frac{\nu}{1.4\,{\rm GHz}}\right)^{-1}. \tag{64}$$

Here, there is uncertainty in $\epsilon_{\rm r}$ and $\nu$. With the Square Kilometer Array (SKA1), whose sensitivity is $\sim$1 mJy for 0.35–1.05 GHz (SKA1-MID band 1) and 0.95–1.76 GHz (SKA1-MID band 2) [67,68], we can observe the radio precursor at 100 Mpc for $\epsilon_{\rm r} > 2\times10^{-4}$. In estimating the sensitivity, we assume that the pulse duration is 10 ms and the bandwidth is 100 MHz. We note that the field of view of SKA will be $\sim$200 deg$^2$ and approximately 5% of the all sky is covered. Therefore, the detection of the radio precursor by chance is unlikely, and prediction of the sky position is important to detect it. However, if the BH in a BH–NS binary is rapidly spinning, the prospect for detection is enhanced because a close orbit is possible and the luminosity can be $\sim10^{42}\,{\rm erg\,s^{-1}}$ at 1 ms before the merger.

If the value of the efficiency can be as high as $\epsilon_{\rm r} \sim 0.1$, the flux density is approximately $F_\nu \sim 0.5\,{\rm Jy}$, which is comparable to typical FRBs. The radio wave emission from the magnetosphere induced by the orbital motion can be a candidate for the unknown sources of FRBs if the efficiency for the radio emission is extremely high or the BH is highly spinning. We note that the BNS merger event rate is smaller than the FRB event rate, and thus only a small fraction of the FRBs can be explained by NS mergers [69,70].

The effect of plasma can modify the propagation of radio waves in the magnetosphere induced by the orbital motion. We consider the plasma frequency. Electromagnetic waves with a frequency below the plasma frequency $\nu_{\rm p}$ cannot propagate through the plasma [71]. Using Eq. (61), the plasma frequency at $r = c/\Omega$ is

$$\nu_{\rm p} \simeq 200\,{\rm MHz}\left(\frac{B}{10^{12}\,{\rm G}}\right)^{1/2}\left(\frac{M_{\rm c}}{10\,M_\odot}\right)^{5/4}\left(\frac{a}{90\,{\rm km}}\right)^{-13/4} \tag{65}$$

$$\simeq 170\,\mathrm{MHz}\left(\frac{B}{10^{12}\,\mathrm{G}}\right)^{1/2}\left(\frac{M_\mathrm{c}}{10\,M_\odot}\right)^{7/16}\left(\frac{M_\mathrm{tot}}{11.4\,M_\odot}\right)^{-13/16}\left(\frac{t}{10\,\mathrm{ms}}\right)^{-13/16}, \quad (66)$$

where we set the radius of the NS as $R_\mathrm{NS} = 12\,\mathrm{km}$ and the multiplicity of the magnetosphere as 1. Ordinary-mode radio waves, with frequency below $\nu_\mathrm{p}$, cannot propagate through the magnetosphere. Because the plasma frequency is proportional to the square root of the plasma number density, an ordinary-mode radio wave with frequency of order 1 GHz is not able to propagate through the plasma when the multiplicity is larger than ∼25. Under a strong magnetic field, the X-mode of radio waves with frequency $\nu < \nu_\mathrm{p}$ can propagate in the plasma. This effect can make it easier for low-frequency radio waves to propagate in the magnetosphere.

Free–free absorption also disturbs the propagation of radio waves. For radio waves with frequency $\nu$ and size of the source $l \sim 100\,\mathrm{km}$ (comparable to $c/\Omega$), we obtain the optical depth for radio waves as [71]

$$\tau \simeq 6\times 10^{-6}\left(\frac{\gamma}{10^2}\right)^{-3/2}\left(\frac{n_e}{10^{12}\,\mathrm{cm}^{-3}}\right)^2\left(\frac{\nu}{1\,\mathrm{GHz}}\right)^{-2}\left(\frac{l}{100\,\mathrm{km}}\right), \quad (67)$$

where $\gamma$ is the Lorentz factor of the plasma particle in the magnetosphere, and the multiplicity of the magnetosphere is assumed to be 1. The optical depth is smaller than 1 and thus free–free absorption would not shield the radio wave. We note that if we assume $\gamma \sim 100$, the radio wave with $\nu = 1\,\mathrm{GHz}$ is in the small-angle uncertainty principle range and the velocity-averaged Gaunt factor is approximately $\bar{g}_\mathrm{ff} \sim 17$ [72]. In the situation that the multiplicity is larger than order $10^3$, the optical depth becomes larger than 1 and the radio wave would be blocked. If the motion of the plasma is restricted by a strong magnetic field, it is known that the optical depth of the free–free absorption becomes smaller than Eq. (67) [73]. This effect can make it easier for radio waves to propagate in the magnetosphere.

In radio pulsars, the temporal variation of the linear polarization position angle of the pulses contains information about the projected magnetic field orientation in the emission region. With this variation, we can constrain some geometrical parameters of the emission regions such as inclination and radial distance measured from the center of the pulsar [74,75]. In the binary case, if these kinds of temporal variation are observed, we might be able to constrain the geometrical features of the emission region, such as radial distance, opening angle of the emitting cone, and the inclination of the magnetic dipole moment with respect to the orbital angular momentum. Our analytic solution and the gravitational wave signal can help to constrain these parameters.

### *3.2.2. Gamma-ray and X-ray emission*

Next, we consider the observability of X-ray or gamma-ray precursors. From pulsar magnetospheres, gamma-rays or X-rays can be emitted. Gamma-ray pulsars emit gamma-rays with a fraction from $10^{-3}$ to 1 of the spin-down luminosity [58–61]. Like X-ray emission from ordinary pulsars, binaries just before merger may emit X-rays and gamma-rays.

If we assume that all photons have the same energy $\epsilon$, the photon number flux is

$$F_\mathrm{ph} = 2.6\times 10^{-7}\,\mathrm{cm}^{-2}\,\mathrm{s}^{-1}\left(\frac{\epsilon_{\mathrm{X},\gamma}}{1}\right)\left(\frac{L}{5\times 10^{40}\,\mathrm{erg\,s}^{-1}}\right)\left(\frac{\epsilon}{100\,\mathrm{keV}}\right)^{-1}\left(\frac{D}{100\,\mathrm{Mpc}}\right)^{-2}, \quad (68)$$

where $\epsilon_{\mathrm{X},\gamma}$ is the efficiency of X-rays or gamma-rays. Therefore, in hard X-ray (∼100 keV), the Swift Burst Alert Telescope (BAT), whose sensitivity is $\sim 10^{-8}\,\mathrm{erg\,cm}^{-2}\,\mathrm{s}^{-1}$ at 15–150 keV [76], is

able to observe the precursor if the strength of the magnetic field $B$ is stronger than $\sim 10^{14}$ G and the efficiency $\epsilon_\gamma$ is $\sim 1$. Also, the *Fermi* Gamma-ray Burst Monitor (GBM), whose trigger sensitivity is $\sim 0.7\,\mathrm{cm}^{-2}\,\mathrm{s}^{-1}$ at 50–300 keV [77], is able to observe the X-ray precursor if the strength of the magnetic field $B$ is stronger than $\sim 10^{15}$ G and the efficiency $\epsilon_\mathrm{X}$ is $\sim 1$ or the BH in a BH–NS binary is so rapidly spinning that an orbital radius with $R \sim M_\mathrm{BH}$ is possible. For a typical NS magnetic field, $B \sim 10^{12}$ G, and a moderately spinning BH in a BH–NS binary, it is difficult to observe the precursor in hard X-rays and gamma-rays. Thus, observation of the precursor in gamma-rays and X-rays is not very likely, although this possibility cannot be completely excluded.

### 3.2.3. *Particle wind*

The particle-in-cell simulation in Ref. [78] shows that magnetic reconnection at current sheets could accelerate charged particles up to $\gamma \sim \sigma_\mathrm{LC}$ in a pulsar magnetosphere. Here, $\gamma$ is the Lorentz factor of the accelerated particles and $\sigma_\mathrm{LC}$ is the sigma parameter of the pulsar at $r \sim c/\Omega$. Like the case in this simulation, the charged particles could be accelerated via magnetic reconnection in the magnetosphere induced by the orbital motion, and particle wind could be ejected. The luminosity of the wind has the same parameter dependence as the Poynting flux, as shown below.

Here, we estimate the order of the luminosity of the particle wind. The accelerated particles are expected to be ejected mainly from the tail part of the spiral arm which is located at $r = c/\Omega$. The orbital motion would eject particles from the tail part of the magnetosphere and the ejection would create some vacuum gap in the magnetosphere. From Eq. (60), the charge density of the plasma at $r = c/\Omega$ is

$$\rho_\mathrm{c} \simeq \frac{(a\Omega B_\mathrm{dip})\Omega}{4\pi c^2}\left(\frac{R_\mathrm{NS}}{c/\Omega}\right)^3. \tag{69}$$

The total radiated charge per second, $I$, is $\sim \rho_\mathrm{c} \times 4\pi(c/\Omega)^2 c$. We assume that these particles are accelerated by an electromotive force $\Delta\Phi$, so the total luminosity is written as

$$L_\mathrm{wind} \sim \rho_\mathrm{c}\, 4\pi \left(\frac{c}{\Omega}\right)^2 c\Delta\Phi. \tag{70}$$

Because the system is dynamical, it is not easy to estimate the electromotive force between the magnetic field lines. Thus, to know the order of the maximum electromotive force which accelerates the charged particles in the magnetosphere, we assume

$$\Delta\Phi \sim E_\mathrm{LC}\frac{c}{\Omega} \sim \frac{a\Omega}{c}B_\mathrm{LC}\frac{c}{\Omega} \sim a\frac{B_\mathrm{dip}R_\mathrm{NS}^3}{(c/\Omega)^3}, \tag{71}$$

where $E_\mathrm{LC}$ denotes the electric field strength at $r = c/\Omega$. Then, we get the total luminosity as

$$L_\mathrm{wind} \sim 6\times 10^{40}\,\mathrm{erg\,s^{-1}}\left(\frac{B_\mathrm{NS}}{10^{12}\,\mathrm{G}}\right)^2\left(\frac{R_\mathrm{NS}}{12\,\mathrm{km}}\right)^6\left(\frac{M_\mathrm{c}}{10\,M_\odot}\right)^2\left(\frac{M_\mathrm{c}+M_\mathrm{NS}}{11.4\,M_\odot}\right)\left(\frac{R}{90\,\mathrm{km}}\right)^{-7}. \tag{72}$$

Here, $R$ is the separation of the binary. This luminosity is comparable to the total Poynting flux in Eq. (36) and has the same parameter dependence as $L_\mathrm{dip}$. Since the energy of the particle wind increases as the separation of the binary shrinks (see Eq. (71)), the particles ejected just before the merger could have higher energy.

## 4. Summary and discussion

In this paper we analytically solve the electromagnetic field around binary compact stars containing at least one NS, and study the properties of the electromagnetic field. Assuming vacuum, we solve Maxwell's equations with the source term of a magnetic dipole moment, using the vector spherical harmonics expansion and Green's function for the Sturm–Liouville problem. We show that the electromagnetic field is characterized by a spiral arm with high energy density (see Fig. 1). This configuration is due to the enhancement of the electromagnetic field not only by the dipole modes but also by the the higher multipole modes. The higher multipole modes also enhance the total luminosity at infinity by a factor of 2–4 just before the merger of the binary (see Eq. (36) and Fig. 5). Also, we show that the direction of the magnetic fields steeply changes at both edges of the spiral arm (see Figs. 1 and 2). In such regions, magnetic reconnection could occur in the presence of plasma, as this possibility is verified in Ref. [44].

In addition, we discuss magnetosphere formation in NS binaries in the late inspiral phase. We indicate that a magnetosphere is induced by the orbital motion of magnetized NSs, and estimate the particle number density of the magnetosphere to be approximately $10^{12}\,\mathrm{cm}^{-3}$ for an NS with a $10^{12}$ G magnetic field at its pole (see Eq. (61)). This density is higher than the typical particle number density of the magnetosphere induced by the intrinsic spin of ordinary NSs ($\sim 10^{11}\,\mathrm{cm}^{-3}$ for a pulsar whose magnetic field is $10^{12}$ G and period is 1 s). For ordinary pulsars, the Goldreich–Julian density is induced because the rotation of the velocity of the plasma is not zero ($\vec{\nabla} \times \vec{v} \neq 0$). By contrast, the plasma density of the magnetosphere in NS binaries is induced as a result of the deformation of the magnetic field by the orbital motion, i.e. the acceleration of the magnetized NS ($\vec{\nabla} \times \vec{B} \neq 0$).

Using the radiation formula and the number density of the magnetosphere, we estimate the luminosity of the precursor under the assumption that the radiation efficiency is the same as that of ordinal pulsars. We consider three possibilities as precursors: particle wind, radio pulse, and gamma-ray and X-ray emission. We evaluate the observability of these radiations, and suggest that gamma-ray and X-ray emission is observable by telescopes currently in operation only if the magnetic field of the NS is as strong as that of magnetars or the BH in a BH–NS binary is spinning extremely rapidly. Radio waves can be observable if the radiation efficiency $\epsilon_{\mathrm{r}}$ is as high as $\sim 10^{-1}$ for ordinary BNSs or the BH in a B-H-NS binary is rapidly spinning, and it might be a candidate for some FRBs. Even if $\epsilon_{\mathrm{r}}$ is as small as $2 \times 10^{-4}$, radio waves can be a candidate for observation with SKA-MID in the future.

In the original argument in Ref. [53], they first considered a rotating NS in vacuum and showed that the induced surface electric charge on the NS creates an electric field $E_{\parallel}$ parallel to the magnetic field. This electric field, $E_{\parallel}$, accelerates charged particles from the surface of the NS in vacuum, and the charged particles construct a magnetosphere for the pulsar. Following this argument, we have to consider whether $E_{\parallel}$ exists or not with the surface charge of the NS in vacuum induced by the orbital motion for the discussion of the formation of the magnetosphere. After the formation of the magnetosphere, the magnetic field in the NS is likely to be a dipolar field and not contain the other components, $\vec{B}_{\mathrm{moving}}$ and $\vec{B}_{\mathrm{rad}}$. The difference between the magnetic field in the NS and the outer region might be kept by the surface currents on the NS. However, for simplicity we ignore the difference of the magnetic field in the NS and the outer region. These currents on the surface of the NS might change the magnetic field around the binary, and the modification might be a power series of $\sim R_{\mathrm{NS}}/R_{\mathrm{LC}}$ because this difference is due to the surface condition on the surface of the NS.

To establish a more precise picture of the electromagnetic field and the magnetosphere induced by the orbital motion, we need to perform force-free or particle-in-cell simulations. The key ingredient

of magnetosphere formation is orbital motion whose speed is a few $\times 10\%$ of the speed of light in compact orbits. Therefore, in a simple head-on collision particle-in-cell calculation [35], the configuration of the magnetosphere is not the same as our results. Recently, a force-free simulation for a binary was performed in Ref. [44]. The configuration of the poloidal magnetic field is different from our results because plasma is present (their Fig. 3). In this magnetosphere, Alfvén waves are generated and they interact nonlinearly, resulting in the formation of current sheets and dissipation. Their result shows the presence of a spiral current sheet, and its spiral configuration is the same as the spiral arm in our vacuum solution (their Fig. 2 and our Fig. 1). According to their Fig. 6 that shows the luminosity, the presence of the plasma enhances the total luminosity by a factor of 2.5 from the vacuum luminosity when the velocity of the NS is $0.4c$. Therefore, our vacuum solution can capture the magnetosphere around the orbiting NS, at least qualitatively, and is able to estimate the luminosity within a factor of $\sim 2$ even just before the merger.

**Acknowledgements**

We thank Federico Carrasco for fruitful discussions. We also thank Hamid Hamidani, Wataru Ishizaki, Kazuya Takahashi, Takahiro Tanaka, and Bing Zhang for several helpful discussions. This work is in part supported by Japan Society for the Promotion of Science (JSPS)/MEXT grants nos. 16H02183, JP20H00158 (MS), 20H01901, 20H01904, 20H00158, 18H01215, 18H01213, 17H06357, 17H06362, 17H06131 (KI), and 20J13806 (TW).

## References

[1] B. P. Abbott et al. [LIGO Scientific Collaboration and Virgo Collaboration], Phys. Rev. Lett. **119**, 161101 (2017) [arXiv:1710.05832 [gr-qc]] [Search INSPIRE].
[2] B. P. Abbott et al., Astrophys. J. Lett. **848**, L12 (2017) [arXiv:1710.05833 [astro-ph.HE]] [Search INSPIRE].
[3] B. P. Abbott et al., Astrophys. J. Lett. **848**, L13 (2017) [arXiv:1710.05834 [astro-ph.HE]] [Search INSPIRE].
[4] B. Paczynski, Astrophys. J. **308**, L43 (1986).
[5] J. Goodman, Astrophys. J. **308**, L47 (1986).
[6] D. Eichler, M. Livio, T. Piran, and D. N. Schramm, Nature **340**, 126 (1989).
[7] J. M. Lattimer and D. N. Schramm, Astrophys. J. **192**, L145 (1974).
[8] B. F. Schutz, Nature **323**, 310 (1986).
[9] K. Hotokezaka, E. Nakar, O. Gottlieb, S. Nissanke, K. Masuda, G. Hallinan, K. P. Mooley, and A. T. Deller, Nature Astron. **3**, 940 (2019) [arXiv:1806.10596 [astro-ph.CO]] [Search INSPIRE].
[10] B. P. Abbott et al. [The LIGO Scientific Collaboration and the Virgo Collaboration], Phys. Rev. Lett. **121**, 161101 (2018) [arXiv:1805.11581 [gr-qc]] [Search INSPIRE].
[11] B. P. Abbott et al. [The LIGO Scientific Collaboration and The Virgo Collaboration, The 1M2H Collaboration, The Dark Energy Camera GW-EM Collaboration and the DES Collaboration, The DLT40 Collaboration, The Las Cumbres Observatory Collaboration, The VINROUGE Collaboration, and The MASTER Collaboration], Nature **551**, 85 (2017) [arXiv:1710.05835 [astro-ph.CO]] [Search INSPIRE].
[12] B. P. Abbott et al. Astrophys. J. Lett. **892**, L3 (2020) [arXiv:2001.01761 [astro-ph.HE]] [Search INSPIRE].
[13] I. Bartos, P. Brady, and S. Márka, Class. Quantum Grav. **30**, 123001 (2013) [arXiv:1212.2289 [astro-ph.CO]] [Search INSPIRE].
[14] S. Rosswog, Int. J. Mod. Phys. D **24**, 1530012 (2015) [arXiv:1501.02081 [astro-ph.HE]] [Search INSPIRE].
[15] R. Fernández and B. D. Metzger, Ann. Rev. Nucl. Part. Sci. **66**, 23 (2016) [arXiv:1512.05435 [astro-ph.HE]] [Search INSPIRE].
[16] E. Berger, Ann. Rev. Astron. Astrophys. **52**, 43 (2014) [arXiv:1311.2603 [astro-ph.HE]] [Search INSPIRE].

[17] R. Sari, T. Piran, and R. Narayan, Astrophys. J. Lett. **497**, L17 (1998) [arXiv:astro-ph/9712005] [Search INSPIRE].
[18] L.-X. Li and B. Paczyński, Astrophys. J. Lett. **507**, L59 (1998) [arXiv:astro-ph/9807272] [Search INSPIRE].
[19] B. D. Metzger, Liv. Rev. Rel. **23**, 1 (2019) [arXiv:1910.01617 [astro-ph.HE]] [Search INSPIRE].
[20] S. Kisaka and K. Ioka, Astrophys. J. Lett. **804**, L16 (2015) [arXiv:1503.06791] [astro-ph.HE]] [Search INSPIRE].
[21] K. Ioka and K. Taniguchi, Astrophys. J. **537**, 327 (2000) [arXiv:astro-ph/0001218] [Search INSPIRE].
[22] B. Zhang, Astrophys. J. Lett. **873**, L9 (2019) [arXiv:1901.11177 [astro-ph.HE]] [Search INSPIRE].
[23] S. T. McWilliams and J. Levin, Astrophys. J. **742**, 90 (2011) [arXiv:1101.1969 [astro-ph.HE]] [Search INSPIRE].
[24] M. Lyutikov, Phys. Rev. D **83**, 124035 (2011) [arXiv:1104.1091 [astro-ph.HE]] [Search INSPIRE].
[25] M. Lyutikov, Phys. Rev. D **83**, 064001 (2011) [arXiv:1101.0639 [astro-ph.HE]] [Search INSPIRE].
[26] D. Lai, Astrophys. J. Lett. **757**, L3 (2012) [arXiv:1206.3723 [astro-ph.HE]] [Search INSPIRE].
[27] A. L. Piro, Astrophys. J. **755**, 80 (2012) [arXiv:1205.6482 [astro-ph.HE]] [Search INSPIRE].
[28] D. J. D'Orazio, J. Levin, N. W. Murray, and L. Price, Phys. Rev. D **94**, 023001 (2016) [arXiv:1601.00017 [astro-ph.HE]] [Search INSPIRE].
[29] M. Vietri, Astrophys. J. Lett. **471**, L95 (1996) [arXiv:astro-ph/9609028] [Search INSPIRE].
[30] B. M. S. Hansen and M. Lyutikov, Mon. Not. R. Astron. Soc. **322**, 695 (2001) [arXiv:astro-ph/0003218] [Search INSPIRE].
[31] C. Palenzuela, L. Lehner, M. Ponce, S. L. Liebling, M. Anderson, D. Neilsen, and P. Motl, Phys. Rev. Lett. **111**, 061105 (2013) [arXiv:1301.7074 [gr-qc]] [Search INSPIRE].
[32] C. Palenzuela, L. Lehner, S. L. Liebling, M. Ponce, M. Anderson, D. Neilsen, and P. Motl, Phys. Rev. D **88**, 043011 (2013) [arXiv:1307.7372 [gr-qc]] [Search INSPIRE].
[33] J.-S. Wang, F.-K. Peng, K. Wu, and Z.-G. Dai, Astrophys. J. **868**, 19 (2018) [arXiv:1810.00170 [astro-ph.HE]] [Search INSPIRE].
[34] M. Lyutikov, Mon. Not. R. Astron. Soc. **483**, 2766 (2019) [arXiv:1809.10478 [astro-ph.HE]] [Search INSPIRE].
[35] B. Crinquand, B. Cerutti, and G. Dubus, Astron. Astrophys. **622**, A161 (2019) [arXiv:1812.05898 [astro-ph.HE]] [Search INSPIRE].
[36] E. R. Most and A. A. Philippov, Astrophys. J. Lett. **893**, L6 (2020) [arXiv:2001.06037 [astro-ph.HE]] [Search INSPIRE].
[37] B. D. Metzger and C. Zivancev, Mon. Not. R. Astron. Soc. **461**, 4435 (2016) [arXiv:1605.01060 [astro-ph.HE]] [Search INSPIRE].
[38] P. Amaro-Seoane et al., arXiv:1702.00786 [astro-ph.IM] [Search INSPIRE].
[39] R. Takahashi and T. Nakamura, Astrophys. J. Lett. **596**, L231 (2003) [arXiv:astro-ph/0307390] [Search INSPIRE].
[40] S. Kawamura et al., Class. Quantum Grav. **23**, S125 (2006).
[41] S. Sato et al., J. Phys.: Conf. Ser. **840**, 012010 (2017).
[42] W.-H. Ruan, Z.-K. Guo, R.-G. Cai, and Y.-Z. Zhang, Int. J. Mod. Phys. A **35**, 2050075 (2020) [arXiv:1807.09495 [gr-qc]] [Search INSPIRE].
[43] J. Luo et al., Class. Quantum Grav. **33**, 035010 (2016) [arXiv:1512.02076 [astro-ph.IM]] [Search INSPIRE].
[44] F. Carrasco and M. Shibata, Phys. Rev. D **101**, 063017 (2020) [arXiv:2001.04210 [astro-ph.HE]] [Search INSPIRE].
[45] A. Y. Chen and A. M. Beloborodov, Astrophys. J. Lett. **795**, L22 (2014) [arXiv:1406.7834 [astro-ph.HE]] [Search INSPIRE].
[46] Y. Lyubarsky, Mon. Not. R. Astron. Soc. **483**, 1731 (2019) [arXiv:1811.11122 [astro-ph.HE]] [Search INSPIRE].
[47] A. Philippov, D. A. Uzdensky, A. Spitkovsky, and B. Cerutti, Astrophys. J. Lett. **876**, L6 (2019) [arXiv:1902.07730 [astro-ph.HE]] [Search INSPIRE].
[48] M. Maggiore, *Gravitational Waves*, Vol. 1 (Oxford University Press, Oxford, 2008).
[49] M. Shibata, *Numerical Relativity* (World Scientific, Singapore, 2016).
[50] L. Bildsten and C. Cutler, Astrophys. J. **400**, 175 (1992).
[51] R. Ruffini, J. Tiomno, and C. V. Vishveshwara, Nuov. Cim. Lett. **3**, 211 (1972).
[52] W. G. Dixon, Proc. R. Soc. Lond. A **319**, 509 (1970).

[53] P. Goldreich and W. H. Julian, Astrophys. J. **157**, 869 (1969).
[54] A. K. Harding, arXiv:0710.3517 [astro-ph] [Search INSPIRE].
[55] J. Pétri, J. Plasma Phys. **82**, 635820502 (2016) [arXiv:1608.04895 [astro-ph.HE]] [Search INSPIRE].
[56] B. Cerutti and A. M. Beloborodov, Space Sci. Rev. **207**, 111 (2017) [arXiv:1611.04331 [astro-ph.HE]] [Search INSPIRE].
[57] R. N. Manchester, G. B. Hobbs, A. Teoh, and M. Hobbs, Astron. J. **129**, 1993 (2005) [arXiv:astro-ph/0412641] [Search INSPIRE].
[58] A. A. Abdo et al., Astrophys. J. Suppl. **187**, 460 (2010); **193**, 22 (2011) [erratum] [arXiv:0910.1608 [astro-ph.HE]] [Search INSPIRE].
[59] P. S. Ray et al., arXiv:1205.3089 [astro-ph.HE] [Search INSPIRE].
[60] A. A. Abdo et al., Astrophys. J. Suppl. **208**, 17 (2013) [arXiv:1305.4385 [astro-ph.HE]] [Search INSPIRE].
[61] P. A. Caraveo, Ann. Rev. Astron. Astrophys. **52**, 211 (2014) [arXiv:1312.2913 [astro-ph.HE]] [Search INSPIRE].
[62] S. A. Olausen and V. M. Kaspi, Astrophys. J. Suppl. **212**, 6 (2014) [arXiv:1309.4167 [astro-ph.HE]] [Search INSPIRE].
[63] D. R. Lorimer, M. Bailes, M. A. McLaughlin, D. J. Narkevic, and F. Crawford, Science **318**, 777 (2007) [arXiv:0709.4301 [astro-ph]] [Search INSPIRE].
[64] J. I. Katz, Prog. Part. Nucl. Phys. **103**, 1 (2018) [arXiv:1804.09092 [astro-ph.HE]] [Search INSPIRE].
[65] T. Totani, Publ. Astron. Soc. Jpn. **65**, L12 (2013) [arXiv:1307.4985 [astro-ph.HE]] [Search INSPIRE].
[66] S. Yamasaki, T. Totani, and K. Kiuchi, Publ. Astron. Soc. Jpn. **70**, 39 (2018) [arXiv:1710.02302 [astro-ph.HE]] [Search INSPIRE].
[67] S. A. Torchinsky, J. W. Broderick, A. Gunst, A. J. Faulkner, and W. van Cappellen, arXiv:1610.00683 [astro-ph.IM].
[68] K. Spekkens et al., arXiv:1911.03250 [astro-ph.IM].
[69] K. Kashiyama, K. Ioka, and P. Mészáros, Astrophys. J. Lett. **776**, L39 (2013) [arXiv:1307.7708 [astro-ph.HE]] [Search INSPIRE].
[70] V. Ravi, Nature Astron. **3**, 928 (2019) [arXiv:1907.06619 [astro-ph.HE]] [Search INSPIRE].
[71] G. B. Rybicki and A. P. Lightman, *Radiative Processes in Astrophysics* (Wiley, Chichester, 1979).
[72] I. D. Novikov and K. S. Thorne, Proc. Summer School Theoretical Physics, Les Houches, p. 343 (1973).
[73] P. Kumar, W. Lu, and M. Bhattacharya, Mon. Not. R. Astron. Soc. **468**, 2726 (2017) [arXiv:1703.06139 [astro-ph.HE]] [Search INSPIRE].
[74] V. Radhakrishnan and D. J. Cooke, Astrophys. Lett. **3**, 225 (1969).
[75] J. Dyks, B. Rudak, and A. K. Harding, Astrophys. J. **607**, 939 (2004) [arXiv:astro-ph/0307251] [Search INSPIRE].
[76] S. D. Barthelmy et al., Space Sci. Rev. **120**, 143 (2005) [arXiv:astro-ph/0507410] [Search INSPIRE].
[77] C. Meegan et al., Astrophys. J. **702**, 791 (2009) [arXiv:0908.0450 [astro-ph.IM]] [Search INSPIRE].
[78] B. Cerutti, A. Philippov, K. Parfrey, and A. Spitkovsky, Mon. Not. R. Astron. Soc. **448**, 606 (2015) [arXiv:1410.3757 [astro-ph.HE]] [Search INSPIRE].